Catalysis Science & Technology

Accepted Manuscript

ROYAL SOCIETY OF CHEMISTRY

www.rsc.org/catalysis

Catalysis
Science & Technology

Cite this: DOI: 10.1039/c0xx00000x

www.rsc.org/xxxxxx

Dynamic Article Links ►

PAPER

In situ controllable assembly of layered double hydroxide based nickel nanocatalysts for carbon dioxide reforming of methane

Zhenxin Xu,[a] Ning Wang,[b] Wei Chu,*[a] Jie Deng[a,c] and Shizhong Luo*[a]

Received (in XXX, XXX) Xth XXXXXXXXX 20XX, Accepted Xth XXXXXXXXX 20XX
DOI: 10.1039/b000000x

How to attain loaded metal nano-cluster catalysts possessing the concurrently boosted reactivity and durability become increasingly important but still remain a tremendous challenge in nanoparticle hetero-catalysis. In our current study, as an example, an Mg-functionalized Ni-based nanohybrids with both a large dispersion and great grain population and the excellent anti-sintering imbedded in a hierarchical mesostructured γ-Al_2O_3 substrate was successfully developed through an easy and reproducible recipe involving an in situ growth mechanism of the Ni-containing layered double hydroxides (LDHs) using alumina substrates as the sole Al^{3+} source, which presents the exceptional reactivity and durability synchronically for recycling the notorious greenhouse gases into sustainable energy source. The combined analysis of catalytic evaluation and various characterization techniques, such as XRD, N_2 adsorption and desorption characterization, FT-IR, TGA, SEM, ICP-AES, XPS, H_2-TPR, CO_2-TPD, TEM, and in situ CH_4/CO_2-TPSR, unravel a strong structure-function interrelationship. The highly reducible and dispersed surface active Ni species greatly enhanced the activation of methane, while the finely tuned surface acidity-basicity property supplied sufficient reactive centers for the CO_2 adsorption/activation. In addition, the reciprocally strengthened dual confinement effects imparted by both the mesoporous γ-Al_2O_3 matrix and the in situ grown LDHs precursors resulted in the extraordinary catalytic stability, without pronounced sintering and/or agglomeration of reactive phases in demanding working conditions.

1. Introduction

Carbon dioxide reforming of methane (CRM), as expressed by equation $CH_4+CO_2=2CO+2H_2$, have become the most significant route for alleviating the growing greenhouse effect and producing versatile energy source (syngas) and clean hydrogen energy during the recent decades.[1-3] As the most broadly studied catalytic systems for this process, noble metals such as Ru, Rh, Pd, Pt and Ir, albeit highly active and stable, have a high price and limited supply, which makes it difficult to satisfy their dramatically increasing needs in a variety of fields, such as, nanocatalysts, nanoelectrics, energy storage/conversion, and medicine.[4] Recently, transient metals, in particular nickel, anchored onto oxide supports, have been enormously studied as nanocatalysts for CRM due to its low cost, wide abundance, and high reactivity.[5, 6] To recycle greenhouse gases more efficiently, one critical aspect in obtaining the high-performance Ni-based catalysts is to opt for the proper support materials and design the appropriate architecture. In this sense, Al_2O_3, a typical ceramic solid, has received tremendous interests as substrates for supporting Ni nanoparticles owing to its unique physiochemical properties, such as high surface area, mixture of acid-base properties, surface hydration/hydroxylation mechanisms, high mechanical strength, and economical efficiency, which can in theory fulfill the high loading and exceptional catalytic functions.[7]

However, the rapid activity degradation and the inherently high carbon deposition performance of Ni/Al_2O_3 nanocatalysts are the primary hindrance for its realistic applications.[8-10] Thus, intense studies have been concentrated upon improving the CRM catalytic behavior of Ni/Al_2O_3 nanomaterials via enhancing the metal-support synergism and building the Ni-Al_2O_3 nano-architecture. Exemplarily, Wang et al. explored a one-pot solution-phase methodology to fabricate the Ni/ordered mesoporous Al_2O_3 compounds, which could be competent to achieving 80 h stability at 700 °C with the conversion and selectivity both above 80 %.[11] Xu et al. prepared the ordered mesoporous NiO-Al_2O_3 composite oxides, displaying the satisfying reactivity.[12] Furthermore, Kang et al. recently synthesized the Ni@Al_2O_3 core-shell structure through a sol-gel chemistry method, presenting the high stability.[13] Nevertheless, these strategies required complicated and/or eco-unfriendly procedures to accomplish the desired structures. Besides, inspired by benefits of the nano-confined crystallization mechanism of catalyst precursors within limited spaces, the abundant mesopores of Al_2O_3 can be ideally used as a substrate to confine catalyst precursors for generating the small-sized and homogeneously disturbed Ni-containing mixed oxides. For instance, Liu et al. synthesized the La_2NiO_4/γ-Al_2O_3 composites, which were active and stable for CRM.[14] Unfortunately, hydrophilic Al_2O_3 surfaces tend to weakly interact with precursors especially under acidic environment and, thus, cause the agglomeration of precursors and the resulting pore blocking. Meanwhile, Al_2O_3 is a kind of acid oxide and has the weak absorption of such basic reactants such as CO_2 molecules, thereby limiting its usage in catalytic systems wherein basic active centers are needed, e.g, CRM.[15] Hence, there is still far from matching the demand for the next-generation economy-oriented Ni/Al_2O_3 nanocatalysts with extraordinary catalytic functions even after the long-time catalytic cycle.

Layered double hydroxides (LDHs) are a class of ionic lamellar compounds composed of the positively charged brucite-like layers with an interlayer region containing charge compensating anions and solvation molecules.[16] As a layered material, LDH crystallites tend to have a typical morphology with hexagonal platelets. The metal cations occupy the centers of edge sharing octahedra, whose vertexes contain hydroxide ions that connect to form infinite 2D sheets.[17] The most enormously researched LDHs include both divalent and trivalent metal cations, a generic formula for these LDHs may be written as $[M^{2+}_{1-x}M^{3+}_{x}(OH)_2][A^{n-}]_{x/n}\cdot zH_2O$, where M^{2+} may be common Mg^{2+}, Zn^{2+}, or Ni^{2+} and M^{3+} may be common Al^{3+}, Ga^{3+}, Fe^{3+}, or Mn^{3+}. A^{n-} is a nonframework charge compensating inorganic or organic anion, e.g. CO_3^{2-}, Cl^-, SO_4^{2-}, RCO_2^-, and x is normally between 0.2–0.4. The M^{2+} and M^{3+} cations are uniformly and orderly dispersed within layers in the lattice of LDHs.[18, 19] When used as the catalyst precursors, the ordered layer structure after a thermal treatment can be transformed into the mixtures of metal oxides (layered double oxides, LDOs), which have the high thermal stability, and meanwhile the vaporization and decomposition of H_2O, A^{n-} and OH^- can yield well dispersed metallic species and large surface areas.[20-23] Nonetheless, the high anti-coking and -growth could not be achieved merely employing this type of materials due to the facile agglomeration of nanoplates during elevated temperature calcination.

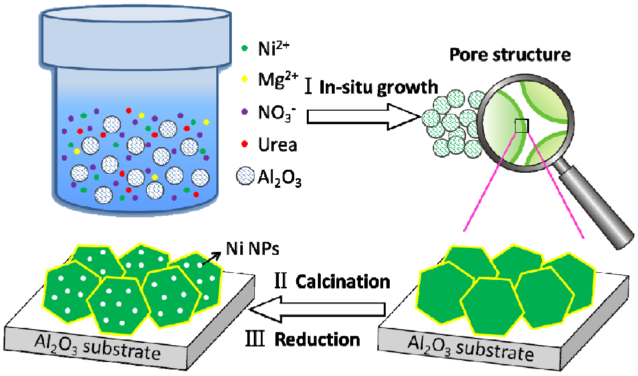

Fig. 1 Schematic illustration of the catalysts derived from LDHs in situ grown on alumina substrate

Based upon forgoing discussions, the LDHs and commercial Al_2O_3 possess the markedly different benefits and the corresponding handicaps. Herein, we developed a catalyst by means of an integration of LDHs ensemble with commercial mesostructured γ-Al_2O_3 module. In a typical procedure, as illustrated in Fig. 1, the mesoporous γ-Al_2O_3 was activated by urea hydrolysis in the solution of the metal nitrates under hydrothermal conditions, and, after a homogeneous co-precipitation process, NiAl-LDH and NiMgAl-LDH were in situ grown on the surface of the γ-Al_2O_3. Such modular engineering can make full use of their advantages but avoid their respective drawbacks. When evaluated for CRM, this hierarchically designed catalysts present the high reactivity as well as the significantly boosted coking-and aggregation-tolerance. This exceptional behavior might arise from the following factors. First, the mesoporous γ-Al_2O_3 with high specific surface area and excellent physical strength was used as both catalyst support and sole source of Al^{3+}, and its mesoporous structure introduced one confinement effect,[24] which effectively limited the deposition of coke and the sintering of the active nickel species. Second, in situ grown LDHs precursors with small crystallite sizes could reintroduce the other confinement effect on Ni cations, which resulted in the small Ni particles and enhanced the dispersion of Ni species as well as their reducibility and interaction with supports after the calcination, these were beneficial to the catalytic activity. Third, the addition of Mg not only generated more basic sites but also regulated the surface content of Ni species on the catalyst. These three advantages could strengthen one another and render the hierarchically catalysts highly coke-and sintering-immune.

2. Experimental

2.1 Catalysts synthesis

For the preparation of the in situ grown LDHs, 5 g γ-Al_2O_3 (Chengdu Kelong Chemical Co., Ltd., China) was impregnated in the aqueous solution of $Ni(NO_3)_2$•$6H_2O$, $Mg(NO_3)$•$6H_2O$ and urea with 10 mL deionized water, and here, the molar ratio of urea to total metal cations was 3:1. After being impregnated for 2 h, the resulting slurry was transferred to an autoclave and aged at 130 °C for 6 h. Then the particles were washed with deionized water until the pH value of the washings reached 7. The resulting NiAl-LDH/γ-Al_2O_3 and NiMgAl-LDH/γ-Al_2O_3 catalyst precursors were gained after drying at 110 °C for 12 h. For comparison, γ-Al_2O_3 (5g) was added in the aqueous solution of $Ni(NO_3)_2$•$6H_2O$ with the 10 mL deionized water and impregnated for 2 h. Then the liquid was evaporated with stirring at 60 °C. Subsequently, all these catalyst precursors were calcined at 500 °C for 3 h in air to obtain the mixed oxides. The mixed oxides derived from LDHs/γ-Al_2O_3 and made by the modified impregnation method were denoted as NiAl-LDO/γ-Al_2O_3, NiMgAl-LDO/γ-Al_2O_3 and NiO-IMP/γ-Al_2O_3, respectively. The Ni content was fixed at 10 wt% in all mixed oxides. Moreover, the amount of MgO for the NiMgAl-LDO/γ-Al_2O_3 was 5 wt%.

NiMgAl-LDH was prepared as a reference sample by means of the traditional co-precipitation method. A 0.4 M aqueous solution of the Ni^{2+}, Mg^{2+} and Al^{3+} nitrates with the molar ratios Ni/Mg/Al = 0.3/2.5/1 was added dropwise to a 0.15 M aqueous solution of Na_2CO_3 at 60 °C with vigorous stirring. During the co-precipitation, the slurry was kept at pH 10.0 by the addition of 1.0 M NaOH solution. Afterwards, the slurry was stirred continuously at 60 °C for 1 h, and aged without stirring at the same temperature for 18 h. The precipitate was washed with deionized water, and then the NiMgAl-LDH was obtained after drying at 110 °C for 12 h. The mixed oxides derived from NiMgAl-LDH by calcination at 500 °C for 3 h were denoted as

NiMgAl-LDO. The Ni content of NiMgAl-LDO was also 10 wt%.

2.2 Characterization

The X-ray diffraction (XRD) analysis was performed using an X-ray diffraction apparatus (Philips X' pert PRO) with Cu Kα (45 kV, 50 mA) radiation. The Scherrer method was employed for the particle size determination. The standard reference material used for Scherrer formula was LaB_6 purchased from China National Institute of Metrology.

Scanning electron microscopy (SEM) analyses of the samples were made using a Hitachi S3400 apparatus with the applied voltage of 20kV.

Room-temperature Fourier transform infrared (FT-IR) spectra were recorded on a Bruker Tensor 27 Fourier transform spectrometer.

The specific surface areas, total pore volumes, and average pore diameters were determined from the N_2 adsorption/desorption isotherms at –196 ^oC, which were measured using an automated surface area & pore size analyzer (Quadrasorb SI apparatus). Before each measurement, the samples were degassed in vacuum at 300 ^oC for 3 h. Specific surface areas of samples were calculated by the Brunauer-Emmett-Teller (BET) method, and the pore size distribution and average pore diameter were determined according to the Barrett-Joyner-Halenda (BJH) method applied to desorption isotherms.

The Ni loading amount in the samples was determined by the inductively coupled plasma atomic emission spectrometry (ICP-AES) using a TJA IRIS Advantage equipment.

The X-ray photoelectron spectroscopy (XPS) were performed using the XSAM800 spectrometer with an Al Kα (hν = 1486.6 eV) X-ray source. The charging effects were corrected by adjusting the binding energy of C 1s peak from carbon contamination to 284.6 eV.

The temperature-programmed reduction with hydrogen (H_2-TPR) was carried out in a fixed-bed reactor. 50 mg sample was loaded, and the reduction gas of 5 % H_2/N_2 was introduced at a flow rate of 30 mL/min. The temperature of the reactor was raised linearly from 100 ^oC to 800 ^oC at a rate of 10 ^oC/min by a temperature controller. The amount of hydrogen consumed was determined on-line using a SC-200 gas chromatograph with a thermal conductivity detector (TCD).

The morphologies of the catalysts were determined visually using a JEOL JEM 2010 transmission electron micro-scope (TEM) operated at 120.0 kV.

The basicity of samples was determined by the temperature-programmed desorption of carbon dioxide (CO_2-TPD). 200 mg of catalyst was treated at 300 ^oC for 1 h in Ar, and CO_2 was then introduced for 1 h at 50 ^oC. After purging with Ar for 1 h to purge the gas line and remove weakly adsorbed CO_2, the sample was heated from 50 ^oC to 800 ^oC with a ramp of 10 ^oC/min and the desorbed CO_2 was detected on-line by a Hiden QIC-20 mass spectrometer. The mass signal at m/z = 44 was used to determine the amount of desorbed CO_2.

The thermo gravimetric analysis was determined with a thermo gravimetric analyzer (TGA Q500). The sample was heated in flowing air from room temperature to 800 ^oC at a heating rate of 10 ^oC/min.

In situ temperature-programmed surface reaction (TPSR) of CH_4 and CO_2 was achieved with a fixed-bed reactor. Before TPSR experiment, the catalyst was reduced under hydrogen flow at 700 °C for 1 h. For CH_4-TPSR experiment, upon cooling down to 50 ^oC under flowing Ar, the CH_4 with a flow rate of 30 mL/min was switched in. The temperature of the reactor was raised linearly to 800 °C at a rate of 10 ^oC/min by a temperature controller. CO_2-TPSR was performed after coking reaction with CH_4 for 30 min at 700 ^oC. The system was cooled down to 50 ^oC in Ar atmosphere. Then the CO_2 gas at a flow reaction rate of 30 mL/min was introduced. The temperature of the reactor was raised linearly to 800 ^oC at a rate of 10 ^oC/min by a temperature controller. The products of CH_4-TPSR and CO_2-TPSR were analyzed on-line by a QIC-20 mass spectrometer.

2.3 Catalytic performance measurements

The catalytic evaluations were performed under atmospheric pressure using a fixed-bed tubular quartz flow reactor (6 mm i.d.). Typically, 100 mg of catalyst was loaded in the reactor. The molar ratio of CH_4 to CO_2 was 1:1, and GHSV was 24,000 mL/(h·g_{cat}). Before the reaction, the samples were reduced in situ with pure H_2 at 700 ^oC for 1 h. The effluent gases from the reactor were analyzed on-line using a GC-1690 model gas chromatograph equipped with a TDX-01 column and a thermal conductivity detector (TCD). The activity tests were evaluated every 50 ^oC over the temperature range of 550-800 ^oC and the stability test was measured for the catalyst with the greatest conversion at 700 ^oC. The conversions of CH_4 (X_{CH4}) and CO_2 (X_{CO2}), the yield of CO (Y_{CO}) and syngas ratios were calculated by using equations (1) – (4):

$$X_{CH_4} = \frac{F_{CH_4,in} - F_{CH_4,out}}{F_{CH_4,in}} \times 100\% \qquad (1)$$

$$X_{CO_2} = \frac{F_{CO_2,in} - F_{CO_2,out}}{F_{CO_2,in}} \times 100\% \qquad (2)$$

$$Y_{CO} = \frac{F_{CO,out}}{F_{CH_4,in} + F_{CO_2,in}} \times 100\% \qquad (3)$$

$$Ratio\ of\ H_2 / CO = \frac{F_{H_2,out}}{F_{CO,out}} \qquad (4)$$

Where $F_{i,in/out}$ was the flow rate of each component in the feed or effluent.

3. Results and discussion

3.1 Catalyst characterization

The XRD patterns of the γ-Al_2O_3 support, the catalyst precursors, NiAl-LDH/γ-Al_2O_3 and NiMgAl-LDH/γ-Al_2O_3, and NiMgAl-LDH, were shown in Fig. 2(a). It could be seen that the support had a γ-Al_2O_3 phase, and that the sharp diffraction peaks at 2θ = 37.6^o, 45.9^o and 67.0^o were observed in Fig. 2(a), which corresponded to the characteristic (311), (400) and (440) reflections of γ-Al_2O_3 phase, respectively. The XRD pattern of NiMgAl-LDH presented the basal spacing (003), higher order (006 and 009) reflections at 2θ = 11.5^o, 23.1^o and 34.7^o, respectively, and the peak around 2θ = 60^o arose from the (110) reflection of LDH phases, similar to those typically reported in the literature.[20, 23] The patterns of NiAl-LDH/γ-Al_2O_3 and NiMgAl-LDH/γ-Al_2O_3 were combinations of the characteristic reflections of γ-Al_2O_3 and those of NiMgAl-LDH as shown in Fig. 2(a), which verified that NiAl-LDH and NiMgAl-LDH had been synthetized successfully on the γ-Al_2O_3 support. The corresponding analyses of XRD were listed out in Table 1. It was interesting to observe that the crystallite size of the hydrotalcite-like precursors grown on the γ-Al_2O_3 was much smaller than that of the direct synthesized LDHs. This could be due to the nanospatially confined crystallization-growth mechanism of LDHs precursors in the limited spaces of the nanoporous γ-Al_2O_3 matrixes.[25] Compared with the NiAl-LDH/γ-Al_2O_3, the intensity of characteristic (003) reflections around $2\theta = 11.5^\circ$ for NiMgAl-LDH/γ-Al_2O_3 was slightly weak, which manifested the decrease in the integrity of the layered structure as a result of the induction of Mg ions.[26] Moreover, the induction of Mg ions also diminished the crystallite size of hydrotalcite-like precursors in direction *a* and *c* for NiMgAl-LDH/γ-Al_2O_3.

Table 1 Structural parameters from XRD of the hydrotalcite-like precursors

Sample	d_{003} (nm)	d_{006} (nm)	d_{009} (nm)	d_{110} (nm)	Lattice parameter[a]		Crystallite size[b] in direction	
					a (nm)	*c* (nm)	*a* (nm)	*c* (nm)
NiMgAl-LDH	0.77	0.38	0.26	0.15	0.30	2.31	15.6	11.2
NiAl-LDH/γ-Al_2O_3	0.76	0.38	0.26	0.15	0.30	2.30	11.8	8.9
NiMgAl-LDH/γ-Al_2O_3	0.76	0.37	0.26	0.15	0.30	2.28	8.8	6.4

[a] The lattice parameters $a = 2d_{110}$ and $c = d_{003} + 2d_{006} + 3d_{009}$. [b] The crystallite sizes in the *a* and *c*-directions calculated using the Scherrer formula from the (110) and (003) reflections, respectively.

The N_2 adsorption-desorption isotherms of the samples were measured to investigate the effects of in situ supported LDHs on the textural properties of γ-Al_2O_3. All the isotherms (Fig. 2(b)) exhibited the type IV isotherm curves with H_3-type hysteresis loops according to the IUPAC classification, which signified the presence of capillary condensation in the mesoporous structure and the newly-created slit-shaped mesopores that resulted from the spatially-orientated array or stacking of plate-like LDHs particles within the γ-Al_2O_3 pore channels.[27] The corresponding textural properties were shown in Table 2. The pore size evolved from a wide distribution of 1.4 ~ 28 nm for γ-Al_2O_3 to a significantly narrow range of 2.8 ~ 17nm for LDHs/γ-Al_2O_3. Moreover, the total pore volumes and the specific area became considerably smaller on LDHs/γ-Al_2O_3 and remained nearly identical for all samples, respectively, which could be attributed to the formation of LDHs microcrystallites on the surfaces of γ-Al_2O_3 pores. Although the crystallites formed clogged up the pores, their plate-like particles with the regular size and well-developed two-dimensional pores did not change the specific surface area significantly.

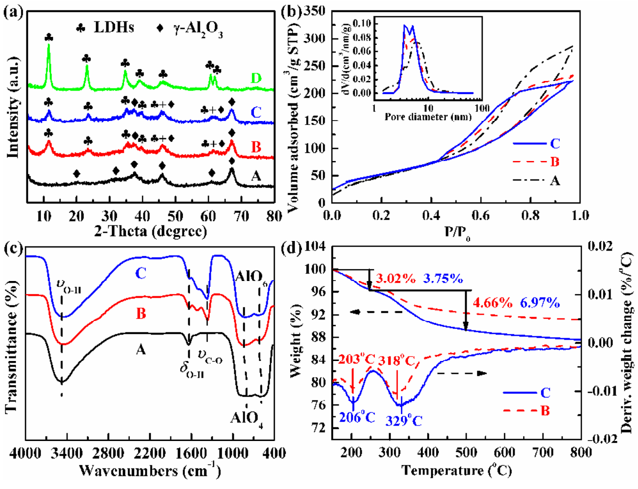

Fig. 2 (a) XRD patterns, (b) N_2 adsorption-desorption isotherms and pore size distributions (inset), (c) FT-IR spectra, and (d) TG/DTG profiles of catalyst precursors: A γ-Al_2O_3, B NiAl-LDH/γ-Al_2O_3, C NiMgAl-LDH/γ-Al_2O_3, D NiMgAl-LDH

Table 2 Textural properties of the samples

Sample	S_{BET}[a] (m^2g^{-1})	V_p[b] (cm^3g^{-1})	D_p[c] (nm)
γ-Al_2O_3	188.7	0.44	9.4
NiAl-LDH/γ-Al_2O_3	189.4	0.36	7.6
NiMgAl-LDH/γ-Al_2O_3	190.6	0.36	7.5

[a] BET specific areas. [b] Total pore volumes were obtained at $P/P_0 = 0.99$. [c] Average pore diameter calculated using the BJH method.

The morphology of samples was characterized by SEM (Fig. 3). There were a large number of petal-like microcrystallites with the good crystallinity and uniform size in the LDHs/γ-Al_2O_3, which further confirmed that the formation of the type IV isotherm curves with H_3-type hysteresis loops in the N_2 adsorption-desorption isotherms (Fig. 2(b)). It was seen that the growth of crystallites in the *ab*-direction all tended to be perpendicular to the γ-Al_2O_3 substrate, which could optimize the growth and avoid the crash among growing crystallites. Furthermore, in accordance with the results from XRD (Fig. 2(a)), the crystallite size of hydrotalcite-like precursors in NiMgAl-LDH/γ-Al_2O_3 was slightly smaller than that in NiAl-LDH/γ-Al_2O_3, and the NiMgAl-LDH/γ-Al_2O_3 exhibited better crystal morphology.

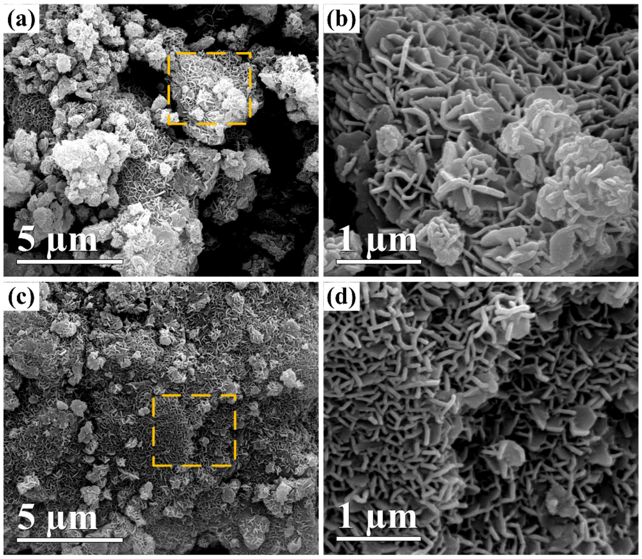

Fig. 3 SEM of (a, b) NiAl-LDH/γ-Al_2O_3 and (c, d) NiMgAl-LDH/γ-Al_2O_3

FT-IR spectra of γ-Al_2O_3, NiAl-LDH/γ-Al_2O_3 and NiMgAl-LDH/γ-Al_2O_3 were displayed in Fig. 2(c). As clearly seen, the adsorption spectra were complex and differed with the catalyst chemical composition and preparation method. The strong and wide peaks between 3600 and 3200 cm^{-1} were related to the hydroxyl stretching band ($\upsilon_{O\text{-}H}$) derived from surface hydroxyl groups and water molecules,[28] while peaks at 1632 cm^{-1} to the bending vibration of water ($\delta_{O\text{-}H}$).[29] This $\upsilon_{O\text{-}H}$ kept nearly the same for every sample. Peaks at 1370 cm^{-1} only appearing upon in situ growing LDHs on γ-Al_2O_3 could be assigned to the C-O ($\upsilon_{C\text{-}O}$) in CO_3^{2-}.[30] This CO_3^{2-} originated from the negatively charged inter-layered CO_3^{2-} in the ionic lamellar brucite-like compounds, which further unequivocally evidenced that the urea hydrolysis and the assembly of ions into the brucite-like layered structure effectively occurred in our designed synthetic recipe. In addition, the peaks at 795 and 605 cm^{-1} on γ-Al_2O_3, which were ascribed to the vibrations of Al-O bond for AlO_4 tetrahedra and AlO_6 octahedra, respectively,[31] obviously shifted upwards to 832 and 830 cm^{-1}, respectively, on the LDHs-containing samples. This shift implied a strong interaction between LDHs crystallites and substrates. Such interaction played a decisive role in controlling the oriented growth of LDHs and their homogeneous distribution in the γ-Al_2O_3 pore surfaces.

As exhibited in Fig. 2(d), the thermo gravimetric analysis (TG/DTG) curves signed two weight loss courses for both NiAl-LDH/γ-Al_2O_3 and NiMgAl-LDH/γ-Al_2O_3. The first weight loss, identified by a DTG peak at around 200 °C, was ascribed to the removal of interlayer water molecules in in situ supported LDHs. The second progress, in which the highest peak emerged at around 320 °C on the DTG curves, corresponded to the dehydroxylation of host-layers and decarbonylation of the interlayer. Although the Mg ions were introduced, the weight loss of water in NiMgAl-LDH/γ-Al_2O_3 was almost the same as that in NiAl-LDH/γ-Al_2O_3, suggesting that two hydrotalcite-like precursors had the same amount of interlayer water. However, the temperature and weight loss in the second progress of NiMgAl-LDH/γ-Al_2O_3 were both larger than that of NiAl-LDH/γ-Al_2O_3. These could be due to that the incorporation of Mg ions enhanced the electrostatic interaction between host-layers and anions of guest interlayer and increased the amount of host-layers hydroxyl together with interlayer carbonate ions.

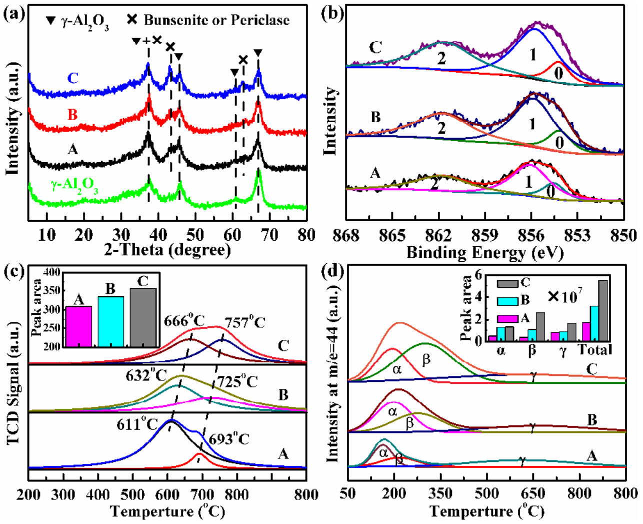

Fig. 4 (a) XRD patterns, (b) Ni $2p_{3/2}$ XPS spectra, (c) H_2-TPR profiles and H_2 consumption peak area (inset), and (d) CO_2-TPD profiles and CO_2 peak area (inset) of samples: A NiO-IMP/γ-Al_2O_3, B NiAl-LDO/γ-Al_2O_3 and C NiMgAl-LDO/γ-Al_2O_3

The phase analyses of the mixed oxides obtained after calcination were generated by XRD (see Fig. 4(a)). Compared to the support γ-Al_2O_3, there were two distinct peaks around 42.9° and 63.0° in the catalysts, which revealed the formation of the bunsenite-type phase (NiO) on the support. Nevertheless, the signals of these two peaks in the NiMgAl-LDO/γ-Al_2O_3 were stronger than that in other catalysts. This certified that the periclase compounds (MgO) could be formed by the introduction of Mg since the diffraction peaks of bunsenite and periclase were very close. Although the spinel-like compound was not detected, the presence of spinel structure containing Mg or Ni or both was not excluded absolutely because this phase could be crystallized deficiently under the calcination of 500 °C.[23]

Table 3 Ni elemental analysis and Ni particle sizes of the samples

Sample	Ni loading (wt%)	Percentage of peak area (%)			Ni at%[a]	Ni particle sizes[b]	
		Peak 0	Peak 1	Peak 2		Reduced	Spent
NiO-IMP/γ-Al_2O_3	9.3	15.0	49.7	35.3	4.7	8.8	15.3
NiAl-LDO/γ-Al_2O_3	9.7	12.2	51.5	36.3	8.3	7.5	9.2
NiMgAl-LDO/γ-Al_2O_3	9.6	10.0	53.8	36.2	9.5	6.2	7.6

[a] The atom percent of surface Ni elemental on the catalysts. [b] Ni particle sizes of reduced and spent samples determined by XRD calculated from the diffraction peak (200).

Surface elemental analysis of the catalyst was performed by XPS. As presented in Fig. 4(b), XPS spectrum about the Ni $2p_{3/2}$ region of mixed oxides all contained three peaks denoted as peak 0, peak 1 and peak 2, which appeared at binding energies around 854, 856 and 862 eV, respectively. These peaks indicated that there were two different Ni species on γ-Al_2O_3: the peak 0 at around 854 eV was assigned to the NiO dispersed on the support,[32] the peak 1 located at around 856 eV could belong to the Ni–Al spinel ($NiAl_2O_4$),[33] which had strong interactions with the support,[34] and the peak 2 was the satellite peak. The percentage of peak area for each peak, as well as the atom percent of surface Ni element on the catalyst was shown in Table 3. The percent of peak areas for peak 1 and peak 2 from LDOs/γ-Al_2O_3 were both more than that from NiO-IMP/γ-Al_2O_3, indicating that the interaction between Ni species and γ-Al_2O_3 in LDO/γ-Al_2O_3 was much stronger than that in NiO-IMP/γ-Al_2O_3. The atom percent for surface Ni on both LDO/γ-Al_2O_3 were also greater than that for NiO-IMP/γ-Al_2O_3. Since the Ni loading amount determined by ICP was essentially the same in these samples (Table 3), this demonstrated that the in situ grown LDHs after calcination enriched the dispersion of Ni species on the surface of γ-Al_2O_3 support.

Fig. 4(c) presented the H_2-TPR profiles of the synthesized oxides. Every catalyst fitted two H_2 consumption peaks with the different temperatures attributed to the reduction of different species. The reduction temperature of the first peak was higher than that of the bulk NiO at 350 °C,[35] indicating the reduction of NiO which had a strong interaction with the support. The second peak above 690 °C was associated with the reduction of Ni-containing spinel $NiAl_2O_4$ or $Ni(Mg)Al_2O_4$.[36, 37] The reduction temperature and its peak area of LDOs/γ-Al_2O_3 were higher than that of NiO-IMP/γ-Al_2O_3, illustrating that the LDOs/γ-Al_2O_3 had the stronger metal–support interaction (SMSI),[12] which was consistent with XPS analysis discussed above. The calculation of H_2 consumption peak area (Fig. 4(c inset)) showed that the peak area of samples became larger successively from NiO-IMP/γ-Al_2O_3 to NiMgAl-LDO/γ-Al_2O_3, so the LDOs/γ-Al_2O_3 had a higher reducibility.

The enriched metal dispersion and reducibility denoted the abundant active sites on the support conducive to the methane activation. The SMSI could inhibit the sintering of Ni during the reaction. For NiMgAl-LDO/γ-Al_2O_3, these properties were all further enhanced after the introduction of Mg.

Fig. 4(d) illustrated the CO_2-TPD profiles of mixed oxides. Three overlapping peaks (α, β, γ) were observed at diverse temperatures, indicating the presence of three kinds of basic sites with different strengths, and the higher the temperature, the stronger the basicity. The α-peak at low temperature was attributed to the release of bicarbonates formed on Brønsted OH^- groups,[38] β-peak at intermediate temperature was associated with the desorption of bidentate carbonates formed on metal-oxygen pairs and γ-peak at high temperature arose from the decomposition of monodentate carbonates formed on low-coordination oxygen anions.[39] The CO_2 desorption peak area through integration revealed that LDOs/γ-Al_2O_3 had more Brønsted OH^- groups and metal-oxygen pairs than NiO-IMP/γ-Al_2O_3. For NiMgAl-LDO/γ-Al_2O_3, the β-peak shifted to 350 °C, and the amount of the metal-oxygen pairs and the low-coordination oxygen anions (γ-peak) was the largest in three samples. These were assigned to the formation of $MgCO_3$ which decomposed at around 350 °C and the oxygen in the Mg^{2+} and O^{2-} pairs, respectively.[40] Moreover, the low-coordination oxygen anions could contribute to facilitating the reaction because the γ-peak was in the range of the reaction temperature. The CO_2 desorption peak area showed the sequence of CO_2 adsorption capacity: NiMgAl-LDO/γ-Al_2O_3> NiAl-LDO/γ-Al_2O_3> NiO-IMP/γ-Al_2O_3. The increased CO_2 adsorption capacity demonstrated the more basic sites and stronger basic characteristics which enhanced the activation of CO_2,[41] and also provided more oxygen species on the surface of catalysts, which was a great help to eliminate carbon species during the reforming process.

The morphology of LDOs/γ-Al_2O_3, which was derived from LDHs/γ-Al_2O_3 by calcination at 500 °C, was characterized by SEM (Fig. 5). It was interesting to find that the morphology of the primary LDHs with the petal-like microcrystallites on the γ-Al_2O_3 support was remained even after the thermal decomposition at high temperature. In agreement with the variation trends of LDHs particle size in the non-calcinated materials, the crystallite size of petal-like microcrystallites in NiMgAl-LDO/γ-Al_2O_3 was still smaller than that in NiAl-LDO/γ-Al_2O_3. Moreover, the LDOs were uniformly dispersed on the support after the high temperature treatment.

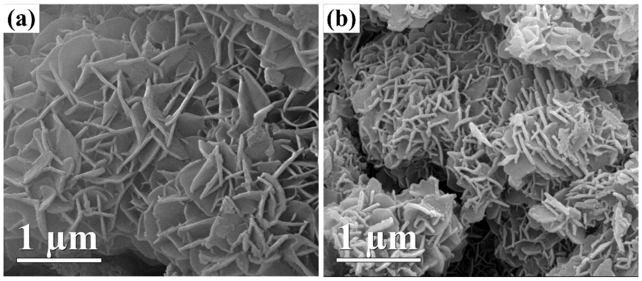

Fig. 5 SEM of (a) NiAl-LDO/γ-Al_2O_3 and (b) NiMgAl-LDO/γ-Al_2O_3

The activations of CH_4 and CO_2, namely the formation and elimination of carbon deposition, were studied by in situ CH_4-TPSR and CO_2-TPSR shown in Fig. 6. The insets in Figure 6 were changes of the signals for H_2 (a) and CO (b) with temperature. The initial activation temperature of methane for NiO-IMP/γ-Al_2O_3 was about 350 °C, while methane over NiAl-LDO/γ-Al_2O_3 and NiMgAl-LDO/γ-Al_2O_3 started to be activated at as low as 320 and 200 °C, respectively. This phenomenon suggested that the methane decomposition (CH_4=C+2H_2) was more easily performed on LDOs/γ-Al_2O_3 samples, which was attributed to their enriched Ni dispersion and reducibility from the analysis of XPS and H_2-TPR. The peak temperature of CO_2-TPSR for NiO-IMP/γ-Al_2O_3 was 763 °C, which was substantially higher than that for NiAl-LDO/γ-Al_2O_3 (741 °C) and NiMgAl-LDO/γ-Al_2O_3 (724 °C). The lower peak temperatures of CO_2 and CO suggested that CO_2 molecule was easier to transport on the metallic site to favor the efficient gasification of the CH_X species formed by the decomposition of methane. This could be caused by the higher basic characteristics of samples according to CO_2-TPD, which enhanced the adsorption and activation of CO_2. Furthermore, this indicated that the carbon species formed on LDOs/γ-Al_2O_3 were more easily eliminated by CO_2 than that on NiO-IMP/γ-Al_2O_3, resulting in the fewer coke produced on LDOs/γ-Al_2O_3 during CRM.

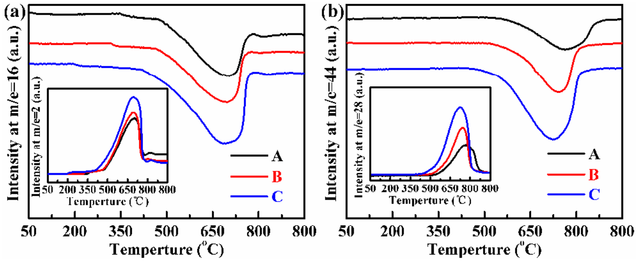

Fig. 6 In situ CH_4-TPSR (a) and CO_2-TPSR (b) of catalysts: A NiO-IMP/γ-Al_2O_3, B NiAl-LDO/γ-Al_2O_3 and C NiMgAl-LDO/γ-Al_2O_3

The TEM images with Ni particle size distributions of the reduced samples, and their XRD patterns were shown in Fig. 7 and Fig. 9(c), respectively. The Ni particle sizes determined by XRD were also listed in Table 3. For these reduced samples in Fig. 9(c), the detected characteristic diffraction peaks of Ni suggested the formation of active metal on the catalysts after reduction at 700 °C for 1 h. Moreover, the Ni diffraction peaks of LDOs/γ-Al_2O_3 were weaker than that of NiO-IMP/γ-Al_2O_3. And as shown in Fig. 7, the size distributions of the Ni particles from LDOs/γ-Al_2O_3 were also much narrower than that from NiO-IMP/γ-Al_2O_3. The weak Ni diffraction peaks and narrow distribution of metal particle size represented a high dispersion of Ni nanoparticles,[42] which verified the previous XPS analysis.

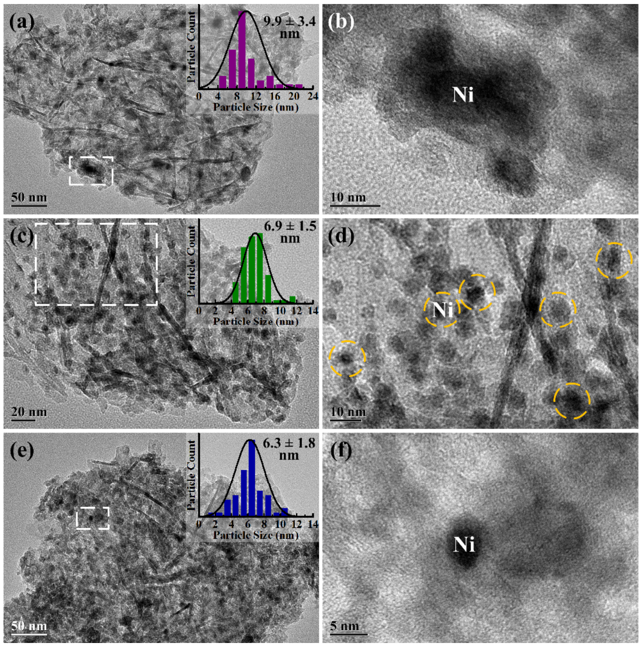

Fig. 7 TEM images and Ni particle size distributions (inset) for catalysts before reaction: (a, b) reduced NiO-IMP/γ-Al_2O_3, (c, d) reduced NiAl-LDO/γ-Al_2O_3 and (e, f) reduced NiMgAl-LDO/γ-Al_2O_3, respectively

The average dimension and size distributions of the Ni particles for all reduced samples were similar to those of the pores for their corresponding precursors (Table 2 and Fig. 2(b)). This indicated that there were dual mutually reinforcing confinement effects in the LDOs/γ-Al_2O_3: one was that the Ni cations were uniformly and orderly distributed in the crystalline host lattice of LDHs precursors, and the other one was from the confinement effect among the mesoporous structure of the γ-Al_2O_3 matrix which generated the in situ grown LDHs precursors with the small crystallite size. The dual confinement effects could contribute to preventing the Ni particles from sintering under severe reduction and reaction conditions. Together with XRD results shown in Table 3, the mean sizes of the Ni particles for reduced LDOs/γ-Al_2O_3 were significantly smaller than that for reduced NiO-IMP/γ-Al_2O_3.

3.2 Catalytic performance

Fig. 8 displayed the catalytic performance of the samples as a function of reaction temperature. There was a significant relationship between the catalytic performance and reaction temperature. As shown in Fig. 8(a) and (b), the conversions of CH_4 and CO_2 for four catalysts increased with the increasing reaction temperature, indicating the endothermic thermodynamic character of CRM. The catalytic conversions on the LDOs/γ-Al_2O_3 were higher than those on NiO-IMP/γ-Al_2O_3 and NiMgAl-LDO in the temperature range of 550-750 °C. The catalysts derived from in situ supported LDHs exhibited higher catalytic activity compared with catalysts from wet impregnation, which was the result of the following factors working together. Primarily, an increase in the surface Ni content of the LDOs/γ-Al_2O_3 improved the reforming activity (Table 3). Secondly, an evident advance in reducibility also enhanced the catalytic activity (Fig. 4(c)). The elevated surface Ni content and reducibility could supply more metal active sites which both facilitated the decomposition of methane and dropped its activation temperature (Fig. 6(a)).[20, 41] Finally, enhanced CO_2 adsorption capacity (Fig. 4(d)) meant the formation of more superficial carbonates, which promoted the transfer of CO_2 molecules to the interface between active metal and support, and then accelerated the conversion of intermediate CH_x species with CO_2 to products. The NiMgAl-LDO/γ-Al_2O_3 showed the most remarkable catalytic activity, with the conversions of CH_4 and CO_2 reaching 80.7% and 79.3% at 700 °C, respectively. This was due to the higher surface Ni content and reducibility and the more and stronger basic sites.

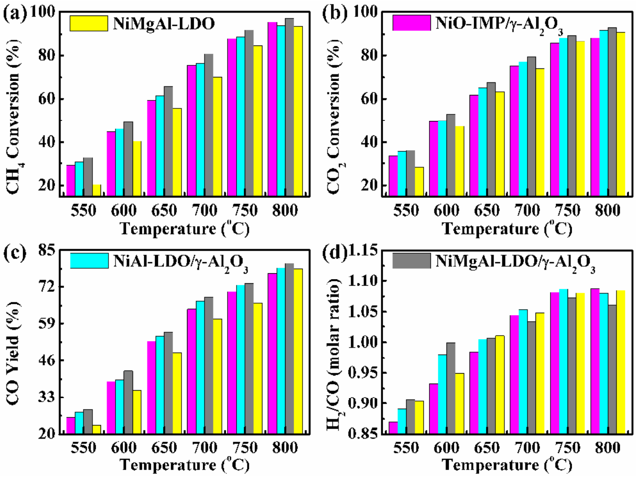

Fig. 8 Effect of reaction temperature on catalytic performance of samples. (Conditions: CO_2/CH_4 = 1:1, GHSV = 24,000 mL/(h·g_{cat}), p = 0.1 MPa)

Compared with the CH_4 conversion, a higher conversion of CO_2 was observed for all catalysts below 700 °C. This was due to the simultaneous occurrence of the reverse water gas shift (RWGS) reaction ($CO_2+H_2=H_2O+CO$). However, for all catalysts, the CH_4 conversion was higher than the CO_2 conversion between 700 and 800 °C. This behavior could be due to the presence of the violent CH_4 decomposition at higher reaction temperatures. This similar phenomenon had also been reported in our previous researches and the literatures by other investigators.[20, 43, 44]

As displayed in Fig. 8(c), the CO yields over LDOs/γ-Al_2O_3 were higher than that on NiO-IMP/γ-Al_2O_3, which could be interpreted as the formation of superficial carbonates due to the more and stronger basic sites of LDOs/γ-Al_2O_3.[45] As discussed above, the superficial carbonates accelerated the reaction of CH_x species with CO_2 as intermediaries and then the CO yields got raised.

The H_2/CO ratio changed between 0.8 and 1.1 at all reaction temperature (Fig. 8(d)), this could be associated with the presence of side reactions such as the RWGS, methanation reactions, and CH_4 decomposition.[11, 20] The ratio on NiMgAl-LDO/γ-Al_2O_3 was closest to the stoichiometric value for the reforming reaction in three samples at each temperature, signifying that there were fewer side reactions occurring on the catalyst during the reaction.

Interestingly, it was found that the catalytic activity of

LDOs/γ-Al_2O_3 below 750 °C, including CH_4 and CO_2 conversions and CO yield, was far higher than that of NiMgAl-LDO. As discussed above, due to the confinement effect of the mesoporous structure of the γ-Al_2O_3 support, the crystallite size of the in situ grown LDHs precursors in LDHs/γ-Al_2O_3 was much smaller than that of the direct synthesized LDHs in NiMgAl-LDH (Table 1). This suggested that the crystallite size of the hydrotalcite-like precursors was an important factor in contributing to promote CRM at lower reaction temperatures for samples derived from LDHs, and the confinement effect of support improved the catalytic performance. Similarly, the positive effect of the small LDHs particle size on the catalytic behavior has been reported before in some significant catalytic systems.[46]

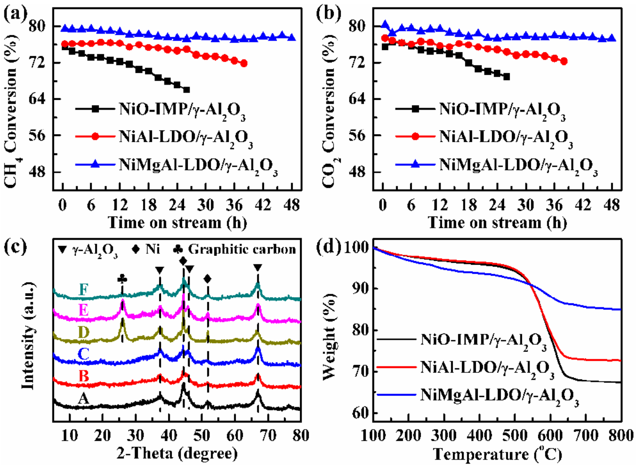

Fig. 9 (a, b) Catalytic stability test of three samples at 700 °C, (c) XRD patterns and (d) TG profiles of spent catalysts after 12 h of TOS at 700 °C: A B C reduced NiO-IMP/γ-Al_2O_3, NiAl-LDO/γ-Al_2O_3 and NiMgAl-LDO/γ-Al_2O_3, and D E F spent NiO-IMP/γ-Al_2O_3, NiAl-LDO/γ-Al_2O_3 and NiMgAl-LDO/γ-Al_2O_3 after 12 h of TOS at 700 °C, respectively

The catalytic stability test was conducted under specific conditions: CO_2/CH_4 = 1:1, GHSV = 24,000 mL/(h·g_{cat}), p = 0.1 MPa, T = 700 °C. As depicted in Fig. 9(a) and (b), during the 48 h on stream, the conversions of reactants for NiMgAl-LDO/γ-Al_2O_3 were extremely stable in the range of 77-80%. It was in line with the stoichiometric coefficient for CRM that the conversion of CH_4 for NiMgAl-LDO/γ-Al_2O_3 was substantially equal to that of CO_2 when they changed with time on stream (TOS). The CH_4 and CO_2 conversions of NiAl-LDO/γ-Al_2O_3 were lower than those of NiMgAl-LDO/γ-Al_2O_3 but higher than those of NiO-IMP/γ-Al_2O_3, which were in agreement with the initial catalytic activity results illustrated in Fig. 8, and they varied less than 5% after 38 h of TOS. However, the catalytic activity of NiO-IMP/γ-Al_2O_3 decreased significantly after only 26 h of TOS, and the CH_4 conversion was reduced by up to 9%. The catalytic stability increased in the following order: NiO-IMP/γ-Al_2O_3< NiAl-LDO/γ-Al_2O_3< NiMgAl-LDO/γ-Al_2O_3.

The spent samples after same 12 h of TOS at 700 °C were analyzed using the XRD and TGA to investigate the reasons for the catalyst deactivation. Due to the presence of side reactions of CH_4 decomposition and CO disproportionation ($2CO=C+CO_2$), coke deposition over the catalyst surface was inevitable.[47] There were different amounts of carbon formation on the three spent samples shown in Fig. 9(c) and (d). The weight loss of spent NiO-IMP/γ-Al_2O_3 was the largest while that of the spent NiMgAl-LDO/γ-Al_2O_3 was the least. This was consistent with the analysis of CO_2-TPD (Fig. 4(d)), indicating that the more basic sites could inhibit the formation of coke. As listed in Table 3, the increase in the size of Ni of LDOs/γ-Al_2O_3 was not significant during the 12 h of TOS, however, the Ni crystallites of spent NiO-IMP/γ-Al_2O_3 grew up to 15.3 nm. These data suggested that the sintering of Ni particles and the coke deposition were the key factors in contributing to the deactivation of the NiO-IMP/γ-Al_2O_3. As shown in Fig. 10, the morphology of the petal-like microcrystallites on the spent LDOs/γ-Al_2O_3 was retained to some extent even under the severe reaction condition during the stability test. However, the destruction of the petal-like structure and the aggregation of the microcrystallites on the spent NiAl-LDO/γ-Al_2O_3 sample were more serious than that on the spent NiMgAl-LDO/γ-Al_2O_3. In addition, there was more filamentous carbon species formed on the spent NiAl-LDO/γ-Al_2O_3 sample. These demonstrated that the addition of Mg was conducive to the stability of the petal-like microcrystallites and the resistance to coking in the LDOs/γ-Al_2O_3.

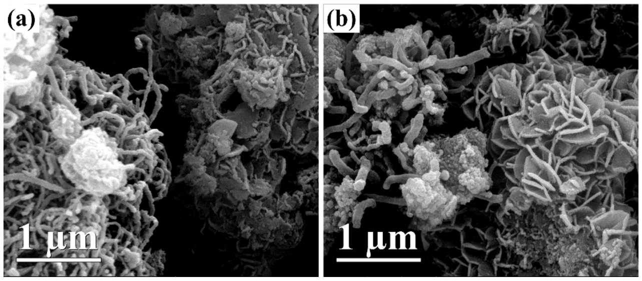

Fig. 10 SEM of (a) spent NiAl-LDO/γ-Al_2O_3 and (b) spent NiMgAl-LDO/γ-Al_2O_3

Overall, all data above indicated that in situ assembling the LDHs into the pores could notably enhance the resistance of Ni-based nanocatalysts to sintering and coking. This improvement could be further reinforced by Mg-functionalization. Clearly, the NiMgAl-LDO/γ-Al_2O_3 composite material could function as a highly efficient and stable nanocatalyst for CRM. More significantly, these functions for the nanomaterials with the nanosheet-in-pore hierarchical structure could be the ideal properties for lots of reactions, e.g., catalytic combustion, cracking, and reforming of hydrocarbons. It can be visualized that these nano-engineered composites here can find a wide usage.

4. Conclusions

A novel composite structure of uniform and small mixed oxide nanoplates embedded onto surfaces of hierarchical mesostructured matrix has been successfully fabricated by the in situ growth strategy using commercial mesoporous alumina as the sole Al^{3+} source, and applied as efficient nanocatalysts for recycling greenhouse gases into renewable energy source under harsh environments. The as-engineered NiMgAl-LDO/mesostructured Al_2O_3 nano-composite is capable of gaining the high initial reactivity while still maintaining satisfactory catalytic stability and excellence resistance to sintering and coking. This remarkable catalytic behavior may be attributable to the unique catalyst architecture and the beneficial synergy between γ-Al_2O_3 and LDOs, namely, uniform distribution, small size of Ni nanoparticles, strong interaction between Ni and support, finely tailored surface acidity/basicity, the dual confinement effects from nanoporous γ-Al_2O_3 supports as well as LDHs precursors, and the intrinsic stability of γ-Al_2O_3 at high temperature. By virtue of both the wide versatility of LDH composition and architecture and of the easiness and reproducibility of in situ growth approach developed here, control over activity and stability of Ni-based catalysts by constructing a nanoplates-on-pore structure displayed in our work can find promising usage in other high-performance metal/oxide nanomaterials for reforming reaction, catalytic combustion, and cracking.

Acknowledgements

This work was supported by the Fundamental Research Funds for the Central Universities (2010SCU22010) and the National Basic Research Program of China (973 Program, No. 2011CB201202). The authors thank Xiaopeng Yu, Bo Xu, Xiangfeng Hu, Wen Yang and Yanyan Feng for their constant encouragements and helpful discussions.

Notes and references

[a] *College of Chemical Engineering, Sichuan University, Chengdu 610065, China. Fax: +86 028 85461108; Tel: +86 028 85403836; E-mail: chuwei1965scu@163.com, Luosz@scu.edu.cn*
[b] *Beijing Key Laboratory of Green Chemical Reaction Engineering and Technology, Department of Chemical Engineering, Tsinghua University, Beijing 100084, China.*
[c] *Department of Chemical Engineering, University of Queensland, Brisbane 4067, Australia.*

1. M. Fan, A. Z. Abdullah and S. Bhatia, *ChemCatChem*, 2009, **1**, 192-208.
2. J. Deng, M. Cai, W. Sun, X. Liao, W. Chu and X. S. Zhao, *ChemSusChem*, 2013, **6**, 2061-2065.
3. D. Liu, Y. Wang, D. Shi, X. Jia, X. Wang, A. Borgna, R. Lau and Y. Yang, *Int. J. Hydrogen Energy*, 2012, **37**, 10135-10144.
4. N. Wang, W. Chu, T. Zhang and Z. Xiu Song, *Int. J. Hydrogen Energy*, 2012, **37**, 19-30.
5. X. Quek, D. Liu, W. N. E. Cheo, H. Wang, Y. Chen and Y. Yang, *Appl. Catal., B*, 2010, **95**, 374-382.
6. X. Yu, F. Zhang, N. Wang, S. Hao and W. Chu, *Catal. Lett.*, 2014, **144**, 293–300.
7. C. Fernández, N. Miranda, X. García, P. Eloy, P. Ruiz, A. Gordon and R. Jiménez, *Appl. Catal., B*, 2014, **156-157**, 202-212.
8. K. Tao, L. Shi, Q. Ma, D. wang, C. Zeng, C. Kong, M. Wu, L. Chen, S. Zhou, Y. Hu and N. Tsubaki, *Chem. Eng. J.*, 2013, **221**, 25-31.
9. I. H. Son, S. J. Lee, A. Soon, H. S. Roh and H. Lee, *Appl. Catal., B*, 2013, **134-135**, 103-109.
10. D. Liu, X. Y. Quek, W. N. E. Cheo, R. Lau, A. Borgn and Y. Yang, *J. Catal.*, 2009, **266**, 380–390.
11. N. Wang, Z. Xu, J. Deng, K. Shen, X. Yu, W. Qian, W. Chu and F. Wei, *ChemCatChem*, 2014, **6**, 1470-1480.
12. L. Xu, H. Song and L. Chou, *Catal. Sci. Technol.*, 2011, **1**, 1032–1042.
13. K. M. Kang, H. W. Kim, I. W. Shim and H. Y. Kwak, *Fuel Process. Technol.*, 2011, **92**, 1236-1243.
14. B. S. Liu and C. T. Au, *Appl. Catal., A*, 2003, **244**, 181-195.
15. L. Sun, Y. Tan, Q. Zhang, H. Xie, F. Song and Y. Han, *Int. J. Hydrogen Energy*, 2013, **38**, 1892-1900.
16. X. Guo, F. Zhang, D. G. Evans and X. Duan, *Chem. Commun.*, 2010, **46**, 5197-5210.
17. Q. Wang and D. O'Hare, *Chem. Rev.*, 2012, **112**, 4124-4155.
18. F. Jing, Y. Zhang, S. Luo, W. Chu and W. Qian, *Appl. Clay Sci.*, 2010, **48**, 203–207.
19. S. He, Z. An, M. Wei, D. G. Evans and X. Duan, *Chem. Commun.*, 2013, **49**, 5912-5920.
20. X. Yu, N. Wang, W. Chu and M. Liu, *Chem. Eng. J.*, 2012, **209**, 623-632.
21. X. Yu, W. Chu, N. Wang and F. Ma, *Catal. Lett.*, 2011, **141**, 1228–1236.
22. W. Luo, F. Jing, X. Yu, S. Sun, S. Luo and W. Chu, *Catal. Lett.*, 2012, **142**, 492–500.
23. C. E. Daza, S. Moreno and R. Molina, *Int. J. Hydrogen Energy*, 2011, **36**, 3886-3894.
24. N. Wang, K. Shen, L. Huang, X. Yu, W. Qian and W. Chu, *ACS Catal.*, 2013, **3**, 1638-1651.
25. J. Feng, Y. Lin, D. G. Evans, X. Duan and D. Li, *J. Catal.*, 2009, **266**, 351-358.
26. M. Li, G. Fan, H. Qin and F. Li, *Ind. Eng. Chem. Res.*, 2012, **51**, 11892-11900.
27. J. A. Foster, D. W. Johnson, M.-O. M. Pipenbrock and J. W. Steed, *New J. Chem.*, 2014, **38**, 927--932.
28. J. J. Murciaa, M. C. Hidalgoa, J. A. Navíoa, J. Aranab and J. M. Dona-Rodríguez, *Appl. Catal., B*, 2013, **142-143**, 205-213.
29. M. Lin, F. Chang and J. Uan, *J. Mater. Chem. A*, 2013, **1**, 14773–14782.
30. K. Bhattacharyya, A. Danon, B. K.Vijayan, K. A. Gray, P. C. Stair and E. Weitz, *J. Phys. Chem. C*, 2013, **117**, 12661-12678.
31. B. Tang, C. Wu, M. Qiu, X. Zhang and S. Zhang, *Mater. Chem. Phys.*, 2014, **144**, 162-167.
32. A. M. Tarditi, N. Barroso, A. E. Galetti, L. A. Arrúa, L. Cornaglia and M. C. Abello, *Surf. Interface Anal.*, 2014, **46**, 521-529.
33. H. Lei, Z. Song, X. Bao, X. Mu, B. Zong and E. Min, *Surf. Interface Anal.*, 2001, **32**, 210-213.
34. I. Gandarias, S. G. Fernández, M. El Doukkali, J. Requies and P. L. Arias, *Top. Catal.*, 2013, **56**, 995-1007.
35. J. Horiguchi, Y. Kobayashi, S. Kobayashi, Y. Yamazaki, K. Omata, D. Nagao, M. Konno and M. Yamada, *Appl. Catal., A*, 2011, **392**, 86-92.
36. Y. Kathiraser, W. Thitsartarn, K. Sutthiumporn and S. Kawi, *Journal of Physical Chemistry C*, 2013, **117**, 8120-8130.
37. G. Wang, Z. Meng, J. Liu, C. Li and H. Shan, *ACS Catal.*, 2013, **3**, 2992-3001.
38. D. P. Debecker, E. M. Gaigneaux and G. Busca, *Chem. Eur. J.*, 2009, **15**, 3920-3935.
39. A. Garcia-Gallastegui, D. Iruretagoyena, M. Mokhtar, A. M. Asiri, S. N. Basahel, S. A. Al-Thabaiti, A. O. Alyoubi, D. Chadwick and M. S. P. Shaffer, *J. Mater. Chem.*, 2012, **22**, 13932–13940.
40. Y. Y. Li, K. K. Han, W. G. Lin, M. M. Wan, Y. Wang and J. H. Zhu, *J. Mater. Chem. A*, 2013, **1**, 12919–12925.
41. X. Du, D. Zhang, L. Shi, R. Gao and J. Zhang, *Nanoscale*, 2013, **5**, 2659-2663.
42. L. Xu, Z. Miao, H. Song, W. Chen and L. Chou, *Catal. Sci. Technol.*, 2014, **4**, 1759–1770.
43. N. Wang, K. Shen, X. Yu, W. Qian and W. Chu, *Catal. Sci. Technol.*, 2013, **3**, 2278--2287.
44. L. Tian, X. H. Zhao, B. S. Liu and W. D. Zhang, *Energ. Fuel.*, 2009, **23**, 607-612.
45. C. E. Daza, C. R. Cabrera, S. Moreno and R. Molina, *Appl. Catal., A*, 2010, **378**, 125-133.
46. J. Wang, Z. Lei, H. Qin, L. Zhang and F. Li, *Ind. Eng. Chem. Res.*, 2011, **50**, 7120-7128.
47. D. Liu, W. N. E. Cheo, Y. W. Y. Lim, A. Borgna, R. Lau and Y. Yang, *Catal. Today*, 2010, **154**, 229–236.

Graphical Abstract

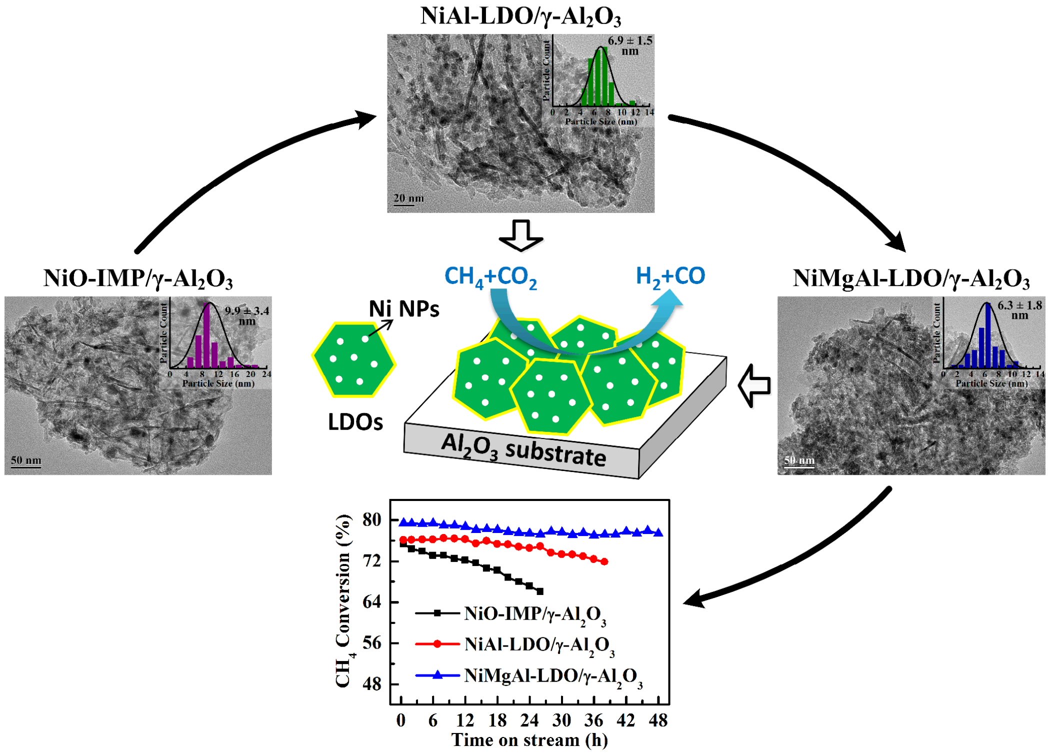

The dual confinement effects from alumina as well as LDHs precursor brought in a new structure of nanoplates-on-pore, with the uniform distribution and smaller size of Ni nanoparticles (NPs) for the LDOs/γ-Al_2O_3, while there were enhanced catalytic performance and better resistances to sintering & to coking.